UNIVERSITI PUTRA MALAYSIA

PHASE FORMATION, CRYSTAL STRUCTURE AND MICROSTRUCTURE OF MgB2 WITH ADDITION OF Se

NUR ZAHIDAH BINTI ABDUL RAHMAN

PHASE FORMATION, CRYSTAL STRUCTURE AND MICROSTRUCTURE OF MgB_2 WITH ADDITION OF Se

NUR ZAHIDAH BINTI ABDUL RAHMAN

BACHELOR OF PHYSICS SCIENCE (HONOURS)

UNIVERSITI PUTRA MALAYSIA

2022

PHASE FORMATION, CRYSTAL STRUCTURE AND MICROSTRUCTURE OF MgB_2 WITH ADDITION OF Se

By

NUR ZAHIDAH BINTI ABDUL RAHMAN

197997

Thesis Submitted to the Department of Physics, Universiti Putra Malaysia, in partial Fulfilment of the Requirements for the Degree of Bachelor of Physics Science (Honours)

January 2022

ABSTRACT

PHASE FORMATION, CRYSTAL STRUCTURE AND MICROSTRUCTURE OF MgB_2 WITH ADDITION OF Se

By

NUR ZAHIDAH BINTI ABDUL RAHMAN

JAN 2022

Supervisor : Chen Soo Kien (Assoc. Prof. Dr.)

Department : Physics, Faculty of Science

The phase formation, crystal structure and microstructure of MgB_2 with the addition of Se was studied in this project. The samples were sintered at 800˚C. X-ray diffraction (XRD) data indicated that MgO was the main phase with a minor amount of MgB_2, MgSe and Se due to the oxidation between Mg and oxygen. The intensity fraction of MgB_2 was found to decrease with the increasing Se addition. The lattice strain of the MgB_2 without addition is higher than the MgB_2 with the addition of Se which is 0.582%. The grain size of sintered MgB_2 with the addition of Se is higher than that of pure MgB_2 indicating higher grain growth of the former. The grain size is 0.4μm and 0.8μm for the MgB_2 without and with addition, respectively. The density of the pure MgB_2 ranged from 1.86g/cm^3 to 1.41g/cm^3 with increasing Se addition.

ABSTRAK

PEMBENTUKAN FASA, STRUKTUR KRISTAL DAN STRUKTUR MIKRO MgB_2 DENGAN TAMBAHAN Se

Oleh

NUR ZAHIDAH BINTI ABDUL RAHMAN

JAN 2022

Penyelia : Chen Soo Kien (Prof. Madya. Dr.)

Jabatan : Fizik, Fakulti Sains

Pembentukan fasa, struktur hablur dan mikrostruktur MgB_2 dengan penambahan Se telah dikaji dalam projek ini. Sampel telah disinter pada 800˚C. Data pembelauan sinar-X (XRD) menunjukkan bahawa MgO adalah fasa utama dengan jumlah kecil MgB_2, MgSe dan Se disebabkan oleh pengoksidaan antara Mg dan oksigen. Pecahan keamatan MgB_2 didapati berkurangan dengan penambahan Se yang semakin meningkat. Ketegangan kekisi MgB_2 tanpa penambahan adalah lebih tinggi daripada MgB_2 dengan penambahan Se iaitu 0.582%. Saiz butiran MgB_2 tersinter dengan penambahan Se adalah lebih tinggi daripada MgB_2 tulen menunjukkan pertumbuhan bijian yang lebih tinggi daripada bekas. Saiz butiran ialah 0.4μm dan 0.8μm untuk MgB_2 tanpa dan dengan penambahan, masing-masing. Ketumpatan MgB_2 tulen adalah antara 1.86g/cm3 hingga 1.41g/cm3 dengan penambahan Se yang semakin meningkat.

ACKNOWLEDGEMENTS

In the name of Allah, the Most Gracious and the Most Merciful.

First and foremost, I would like to express my deepest gratitude and appreciation to my project supervisor, Assoc. Prof. Dr Chen Soo Kien for his guidance, counsel, and support. He is the best supervisor I've had the pleasure of working with, and I'm grateful to have him on my team.

In addition, I would like to express my appreciation to the postgraduate student in the superconductor lab, Miss Nur Hidayah Binti Mohd Hapipi for her guidance and assistance throughout the project. She is a generous and intelligent person who always shared her knowledge in doing experiments and data analysis in this project.

Thank you to my colleague Nurul Atika Farihah Binti Mohd Shafie for helping me a lot throughout the project and I am glad to have her as my partner who supervised under the same supervisor. Besides, I would like to thank Syafiq Husaini who has supported me emotionally and mentally on how I may deliver and give my best through my FYP I and II

Finally, I want to express my gratitude to my family and parents, En. Abdul Rahman Bin Mat, Pn. Marsitah Binti Awi and my sisters for their constant moral support and assistance as I worked on my project. To everyone who was involved in some way with this project, even if they weren't specifically acknowledged here, I would like to say thank you too. I'm grateful for completing this project.

APPROVAL

This thesis entitled the phase formation, crystal structure and microstructure of MgB_2 with the addition of Se by Nur Zahidah Binti Abdul Rahman (Matric No.: 197997) was submitted to the Department of Physics, Faculty of Science, Universiti Putra Malaysia and has been accepted as partial fulfilment of the requirement for the degree of Bachelor of Physics Science (Hons.).

Approved by,

Date: 09 August 2022

……

Assoc. Prof. Dr. Chen Soo Kien
Project Supervisor
Department of Physics
Faculty of Science
Universiti Putra Malaysia

Date:

……

Dr. Md Shuhazlly Mamat@Mat Nazir
Course Coordinator
Department of Physics
Faculty of Science
Universiti Putra Malaysia

Date:

……

Assoc. Prof. Dr. Ts. Suriati Paiman
Head of Deparment
Department of Physics
Faculty of Science
Universiti Putra Malaysia

TABLE OF CONTENT

LIST OF FIGURES

LIST OF TABLES

LIST OF ABBREVIATION

Symbol	Description
˚C	Degree Celcius
Å	Angstrom
a b c	Lattice parameter
AlB_2	Aluminium Diboride
B	Boron
BCS	Bardeen, Cooper, Schrieffer Theory
D	Distance
FWHM	Full width at half maximum
g	Gram
h	Thickness
J_c	Critical current density
m	Mass
MAGLEV	Magnetic levitation
Mg	Magnesium
MgB_2	Magnesium Diboride
MgO	Magnesium Oxide
mol	Mole
MRI	Magnetic resonance imaging
n	Integer
r	Radius
SEM	Scanning electron microscope
Se	Selenium
T_c	Critical transition temperature
V	Volume
XRD	X-ray diffraction
Ɵ	Theta
λ	Wavelength
π	Pi

CHAPTER 1

INTRODUCTION

1.1 Background and history

One of the remaining big frontiers of scientific discovery is superconductors, which are materials that have no resistance to current flow. Superconductivity was first found in the year 1913 when Dutch physicist H. Kamerlingh Onnes of Leiden University was observing materials at absolute zero temperature. As he dropped the temperature, he measured the resistance of a mercury crystal and saw the expected curve of decreasing resistance. However, at 4° Kelvin, the resistance dropped to zero (Bharat, 2018).

In 1933, there was an experiment conducted by Walther Meissner and Robert Ochsenfeld which decreased the temperature near to zero and results in the expulsion of magnetic flux known as the Meissner effect (Gill, 2018). The Meissner effect occurs when a material transitions from a normal to a superconducting state by actively excluding magnetic fields from its interior.

The London equation is one of the theoretical theories for the Meissner effect. Over 20-40 nm, the magnetic field inside the superconductor decays rapidly. The London penetration depth is a parameter that is used to describe it (Nave, 2001). The London Equations were the first successful attempt to characterise superconductors' electrodynamic behaviour in 1935. A critical experiment by Meissner and Ochsenfeld inspired Heinz and Fritz London to create their superconductor theory (Yom, n.d.).

Landau and Ginzburg devised the phenomenological Ginzburg-Landau theory of superconductivity which describes the physical properties of superconductors in 1950. The macroscopic features of superconductors were well explained by this theory, which coupled Landau's theory of second-order phase transitions with a Schrödinger-like wave equation. Abrikosov demonstrated that the Ginzburg-Landau theory predicts the classification of superconductors into Type I and Type II. Bardeen, Cooper, and Schrieffer proposed the entire microscopic theory of superconductivity in 1957. The superconducting current was explained in this BCS theory as a superfluid of Cooper pairs, pairs of electrons interacting through the interchange of phonons (Seeger, 1999).

Researchers at Westinghouse developed the first commercial superconducting wire, a niobium-titanium alloy, in 1962. Josephson made the crucial theoretical prediction that a supercurrent can flow between two pieces of superconductor separated by a thin layer of an insulator in the same year. This phenomenon is now called as Josephson effect. Superconductivity was observed in a lanthanum-based cuprate perovskite material with a transition temperature of 35K by Bednorz and Mueller in 1986 (Seeger, 1999). MgB2 is an "old" material that has been known since the early 1950s, but it was only recently identified by Akimitsu Nagamatsu to be a superconductor at a surprisingly high critical temperature of roughly 40K (Buzea & Yamashita, 2001).

1.2 Type-I superconductors

Type-I superconductors are the pure metals listed in the periodic table except for vanadium, technetium, and niobium. They are also called Soft Superconductors. Type-I superconductors are those which lose their superconductivity rapidly when exposed to an external magnetic field. Type-I superconductors have low critical temperatures and magnetic fields. They show the Meissner effect whereby the magnetic field is unable to penetrate the substance. For type-I superconductors, the transition from a superconducting to a normal state caused by an external magnetic field is sharp and abrupt. Type-I superconductors are not the ideal materials for the production of electromagnets that generate a strong magnetic field due to the low critical magnetic field.

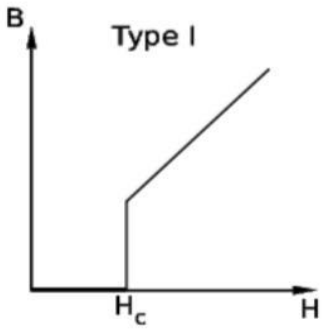

Figure 1.1: The graph of type-I superconductor (Bharat, 2018)

1.3 Type-II superconductors

Type- II superconductors are any superconductors made from alloys and frequently found in a condition that is a combination of normal and superconducting. They are also known as Hard Superconductors. Type-II superconductors are not easily degraded the superconducting state by the external magnetic field. Type-II superconductor has high critical temperature and magnetic field. It is partly obeying the Meissner effect because the magnetic field can penetrate inside the substance. For type-II superconductors, the transition from a superconducting to a normal state because of the external magnetic field is not abrupt. Type-II superconductors start to lose their superconductivity when it at a lower critical magnetic field (Hc_1). When at the upper critical magnetic field (H_{c2}), the type-II superconductor will lose its superconductivity.

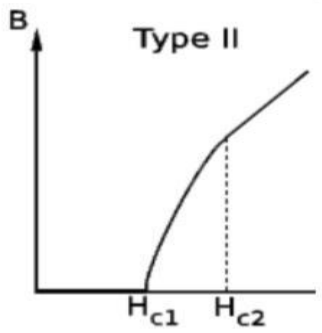

Figure 1.2: The graph of type-II superconductor (Bharat, 2018)

1.4 Applications of superconductor

The development of superconductors has been a benefit to humans and technocrats alike. It has a wide range of applications in science and technology because of its unique zero resistivity feature. It is now employed in telecommunications, medical, transportation, defence, space, and power transfer, among other things. One of the applications of the superconductor is Maglev Train. The function of the Maglev train is to reduce friction and is supported above the tracks by powerful onboard superconducting magnets. It uses high superconductivity to produce a strong magnetic field to support the train. It has a repulsion effect where the magnetic field is partly insulated from the superconductor. Therefore, a magnet and a diamagnet have the same repulsion. On the other hand, it also has an attraction reaction in which the magnetic flux lines that figured out how to infiltrate the superconductor get trapped there by microscopic homogeneities. Magnetic lines penetrate the superconductor by placing the superconductor

close to the magnet that is already hot or forces the magnet to the superconductors. Besides, superconductor has also been used in Magnetic Resonance Image (MRI) for medical application. The non-invasive test magnetic resonance imaging (MRI) is used to diagnose medical disorders. MRI produces comprehensive images of internal body structures using a high magnetic field, radio waves, and a computer. MRI machines have been used every day and each of them contains tens of kilometres of the superconducting wound into a persistent current solenoid. The magnetic field is relatively stable once the current has been stored in the superconducting coil, decreasing by as little as a part per million in a year (Bharat, 2018).

1.5 Problem statement

In recent years, many kinds of chemical doping of MgB_2 have been investigated and reported. At 39 K, MgB_2 becomes a superconductor with one of the highest critical temperatures. To improve the critical current characteristics of MgB_2, numerous elements and compounds have been doped. The best dopants were found to be carbon and silicon-containing compounds which are thought to be the most promising approach to better enhance critical current density performance at high magnetic fields. Up to date, this has not been much research on MgB_2 with the addition of chalcogens, especially selenium and sulphur. With a bigger atomic core and lower electronegativity, selenium is a sister and isoelectronic element of sulphur. The addition of doping Se at the site Mg caused the MgB_2 compound to raise the critical temperature and reduce MgO impurities (Grivel, 2018). The phase formation and crystal structure properties of MgB_2 are also impacted. It is important to investigate the effect of a wider range of Se doping on the crystal structure of MgB_2. For sample preparation, the in-situ method is more effective for the sintering process and doping impurities rather than ex-situ. In this work, samples are prepared by the in-situ solid-state reaction method. The phase formation, crystal structure and microstructure of MgB_2 with the addition of Selenium is studied.

1.6 Objectives

1) To study the effect of Se addition on phase formation of MgB_2.
2) To investigate crystal structure properties in Se added MgB_2.
3) To analyse microstructure evolution of MgB_2 as a result of Se addition.

1.7 Thesis organization

This experiment is carried out to study the phase formation, crystal structure and microstructure of MgB_2 with the addition of Se. Chapter 1 illustrates the background and history of superconductor MgB_2, types of superconductor and applications of superconductor. It is followed by the problem statement and objectives of this project. Chapter 2 outlines the literature review of previous studies on the structure and properties of MgB_2, the effect of additional Se on phase formation of MgB_2 and synthesis of MgB_2. Chapter 3 explains the methodology of this project. It consists of material and apparatus use, the calculation for the raw material, procedures and characterization that used in this project. Chapter 4 shows the results and data obtained using X-Ray Diffraction (XRD), Scanning Electron Microscopy (SEM), Four Point Probe and densimeter. Chapter 5 concludes the research.

CHAPTER 2

LITERATURE REVIEW

2.1 Structure and properties of MgB_2

MgB_2 has been known as a superconductor since the early 1950s but it was just recently been discovered in 2001 by Akimitsu (Nagamatsu et al., 2001). MgB_2 has a high critical temperature of about 39 K. It belongs to the simple hexagonal AIB_2 family with P6/mmm space group. MgB_2 is made up of graphite-type boron layers separated by hexagonal close-packed magnesium layers. Magnesium atoms are found at the centre of hexagons made up of borons, and they contribute their electrons to the boron planes. MgB_2 has a considerable anisotropy in B–B lengths, similar to graphite which the distance between the boron planes is much longer than the inplane B–B distance (Buzea & Yamashita, 2001). Three sigma bonds and two pi bonds make up the band structure of MgB_2. The electronic structure of MgB_2 reveals that it has two conducting bands. Strong two dimensional (2D) covalent and three dimensional (3D) metallic bonding exist between the layers holding the inplane boron atoms together. Both the covalent (2D) sigma band and the metallic (3D) pi band contribute to the electronic density of states at the Fermi level and normal state conductivity (Ravindran et al., 2001).

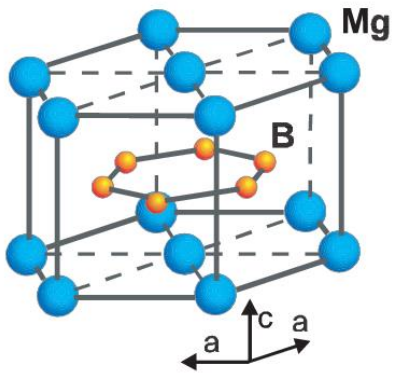

Figure 2.1: Structure of MgB_2 (Buzea & Yamashita, 2001)

MgB_2 was found to be a remarkably high critical temperature superconductor, T_c of 40K for a binary compound. Because it is thought that the metallic B layers play a vital role in the superconductivity of MgB_2, the discovery of superconductivity in MgB_2 validates the predictions of higher Tc in compounds comprising light elements (Kortus 2001). Due to the metallic character of 2D sheets of boron and the high vibrational frequencies of the light boron atoms, MgB_2 has a high critical temperature. Furthermore, MgB_2 also has a high critical current density due when at a low temperature. In comparison to other superconductors, MgB_2 has a

low material cost, a high critical temperature, longer coherence lengths, lower anisotropy, higher critical current densities, higher critical fields, and grain boundaries that are transparent to the current flow, which results in a strong linked current flow in randomly oriented polycrystals and a good fit for both large-scale applications and electrical devices (Buzea & Yamashita, 2001).

2.1.1 Grain boundary of MgB_2

MgB_2 is a low-cost material with a simple structure, low anisotropy, a high Tc, a long coherence length, and transparent grain boundaries. The absence of weak linkages between grain boundaries is an appealing feature of the MgB_2 superconductor, and so an MgB_2 superconductor with a smaller grain size could improve essential features by providing flux pinning centres with a high grain boundary density. Mechanical alloying with HEBM is a successful method for refining precursor powders, resulting in reduced grain sizes, improved reactivity, and an increased surface volume ratio. The irreversibility and higher critical fields are increased by increasing the milling energy supplied to the precursor, resulting in a considerable rise in J_c in the high field region. This is because the smaller the grain size, the higher the surface area of reactivity, and hence the higher the connection at the grain boundary, which produces an increase in J_c on the MgB_2 superconductor.

Kim, et al., and Aksu investigated the effects of heat treatment on the MgB_2 superconductor, including a conventional solid-liquid reaction of 650-1090°C and a solid-state reaction of 600°C below the melting point of Mg (650°C) and the stoichiometric ratio Mg: B = 1:2. They found that there are large composition windows in which Mg liquid and MgB_2 coexist. MgB_2 preparation by conventional and mechanical alloying procedures affects grain size uniformity and density between grains, affecting grain border connectivity and increasing the J_c value of the superconductor MgB_2. Non-homogeneous mixes of MgB_2 powders can be identified as irregular grains. Grain uniformity and density are improved by a visible grain boundary. The grain boundaries have become blurred in some areas, and the grains have melted together (Dewi et al., 2018).

2.1.2 Anisotropy of MgB_2

MgB_2 has a long history of being known for its extremely anisotropic crystalline structure. It seemed probable when specific heat measurements in polycrystalline samples and band structure simulations pointed to the probable anisotropic nature of MgB_2's electrical and magnetic characteristics. In samples of aligned MgB_2 crystallites, the first direct measurement of an anisotropic superconducting property was made for the bulk nucleation field H_{c2}. Some normal state properties, such as compressibility and magnetoresistance, have been shown to have anisotropic behaviour (De Lima, 2002). The bonding of the MgB_2 structure shows a clear anisotropy. The lattice parameter drops quicker along the c-axis with pressure than along the a-axis (Figure 2.2) in all reports, suggesting that out-of-plane Mg–B bonds are substantially weaker than in-plane Mg–Mg bonds. Figure 2.3 shows how the compressibility anisotropy reduces linearly with pressure. The relationship of T_c on the unit-cell volume based on the critical temperature dependence on applied pressure, which was validated by compressibility data. Figure 2.4 shows the curve of $T_c(V)$. Mg–B and B–B bonding lengths are significant in the superconductivity of MgB_2 at such a high T_c compared to other materials, as evidenced by the huge value of critical temperature variation with tiny changes in the unit-cell volume. The critical temperature is reduced by 1K by lowering the unit-cell capacity by only 0.17 $Å^{-3}$ as calculated from Bordet et al's data (2001) and Goncharov et al (2001b). This means that the superconducting properties are extremely sensitive to interatomic distances (Buzea & Yamashita, 2001).

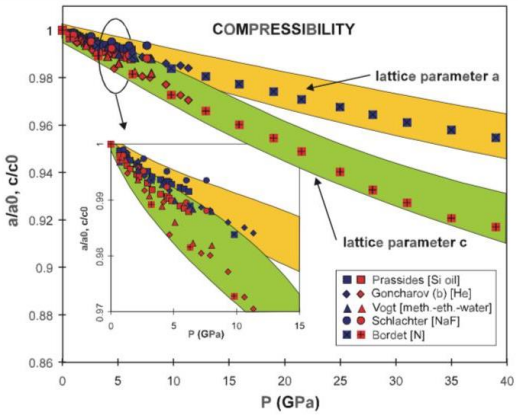

Figure 2.2: The normalized lattice parameters to the zero pressure value versus applied pressure (Buzea & Yamashita, 2001). Data are obtained from Prassides et al (2001) [Si oil], Goncharov et al (2001b) [He], Vogt et al (2001) [meth.–eth.–water], Schlachter et al (2001) [NaF] and Bordet et al (2001) [N]

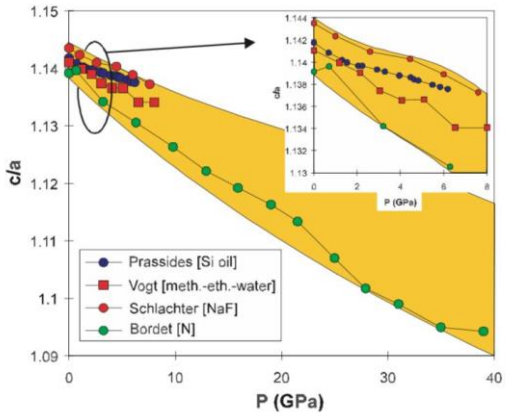

Figure 2.3: The ratio between the lattice parameters along with the c- and a-axis versus pressure (Buzea & Yamashita, 2001). Data are obtained from Prassides et al (2001) [Si oil], Goncharov et al (2001b) [He], Vogt et al (2001) [meth.–eth.–water], Schlachter et al (2001) [NaF] and Bordet et al (2001) [N]

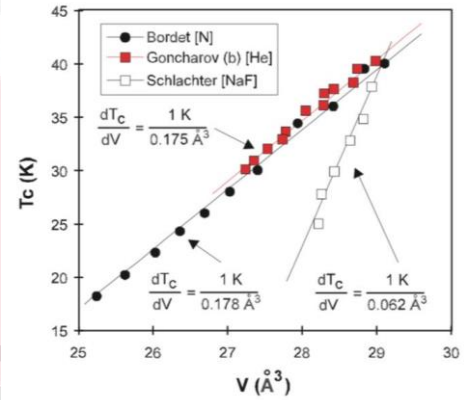

Figure 2.4: The critical temperature of MgB2 versus the volume of the unit cell (Buzea & Yamashita, 2001). Data are obtained from Bordet et al (2001) [N], Goncharov et al (2001b) [He] and Schlachter et al (2001) [NaF]

2.2 Synthesis of MgB_2 using the in-situ method

The two most prevalent methods for fabricating MgB_2 conductors are in-situ and ex-situ which are causing increasing conflicts in terms of connectivity and effective current-carrying cross-sectional area. In the in-situ technique, pure Mg and B powders are mixed in a stoichiometric composition, compressed to the desired form, and then heat-treated to generate the MgB_2 compound. An in-situ reaction produces a strong intergrain coupling with a low packing factor, whereas an ex-situ process using pre-reacted MgB_2 produces tightly packed grains. Some level of MgO impurity is always seen during in-situ mgb2 processing. MgO decreases current flow in the MgB_2 if it forms at grain boundaries (Shcherbakov, 2011). In-situ and ex-situ methods have been used to manufacture MgB_2 bulks, wires, and tapes. Nevertheless, since the intergrain coupling of in-situ MgB_2 is stronger compared with that of the ex-situ one. Besides, the packing factor and connectivity of the in-situ MgB_2 are lower than the ex-situ method. Furthermore, the in-situ reaction is approached when the precursor mixtures of unreacted Mg and B powders. This process causes the ability for sintering to be high and the doping of impurities is effective compared with the ex-situ method (Yamamoto et al., 2012).

2.3 Effect of additional Se on phase formation of MgB_2

It was discovered that adding Se do not affect the formation temperature of MgB_2. The Mg-Se form below 450°C (Grivel et al., 2012). A study has shown the presence of an intermetallic compound (Mg3Bi2) that forms eutectic systems with Mg and Bi with eutectic temperatures of 553°C and 260°C, respectively, is characterised by the Mg–Bi phase diagram described by Nayeb-Hashemi and Clark based on the studies of Grube et al. and Wobst (1961). These characteristics make Bi an appealing additive for lowering the MgB_2 formation temperature since it is more likely to promote Mg melting at lower temperatures than in the pure Mg-B system. Bi is likely to be useful in this view due to its low solubility limit in Mg (maximum 1.12 at. %553°C). The phase diagrams for the Mg-Se systems have yet to be published but given their low melting temperatures (217°C), they appear to be viable candidates for triggering low-temperature liquid formation during the production of MgB_2.

The XRD patterns show at 368°C, much over the melting temperature of Se, the MgSe phase begins to be distinct from the background in the Se doped sample where Se melting between 218°C and 227°C. The additional peak appearing at 227°C in the Se doped sample at

2.32 Å. MgB_2 starts to form around 600°C in the pure Mg-B mixture. Unreacted magnesium is visible up to temperatures of 648°C, and the production of MgB_2 takes place only a short time after the residual Mg is melted. The formation of MgB_2 appears to proceed at the same temperature range in the Se-containing samples. Even though the strength of the diffraction pattern reduces as MgB_2 forms, some Mg3Bi2 is still visible in the diffraction pattern at higher temperatures, indicating that some of this chemical is not involved in the reaction. The amount of MgSe in the Se-added samples does not appear to be altered by MgB_2 production. The Tc of the MgB_2 phase generated with Se additions is similar to the Tc of the pure MgB_2 sample. Se additions even result in a significant reduction in Jc.

SEM pictures in the Se-samples show the smaller particles (less than 1 m) are dispersed throughout the ceramic core. Their size makes determining their composition challenging, although they are most likely MgSe. The presence of the additional elements does not affect the a-lattice parameter of the final MgB_2 phase (a=3.092 Å to3.098 Å depending on the sample –values at 250°C during cooling). The c-axis parameter can also be obtained using the (001) diffraction peak as 3.522 Å and3.527 Å for the undoped and Se-added samples, respectively (Grivel et al., 2012).

CHAPTER 3

METHODOLOGY

3.1 Sample Preparation

Five samples were prepared by using the solid-state reaction technique. A total of 1.6g of pure Magnesium and Boron was used for the first sample. For the second to fifth sample, Selenium powder was added according to the mass calculated in the table. The element has a different mass in each sample due to the different number of moles of Selenium used.

3.1.1 Apparatus

1. Mortar and pestle
2. Spatula
3. Stainless steel tube
4. Furnace
5. Electronic analytical weight balance
6. Hydraulic press
7. Mould and die

3.1.2 Raw Chemical Powder

Table 3.1 Details for raw chemical powder needed

Raw Chemical Powder	Purity (%)	Manufacturer
Magnesium	99.7	Tangshan Wei Hao, China
Boron	95-97	Tangshan Wei Hao, China
Selenium	99.5	Alfa Aesar, USA

3.2 Calculation of Mass for Each Element

Chemical equation of $MgB_2[Se]_x$

Mg + 2B + $xSe \rightarrow$ $MgB_2[Se]_x$

Atomic mass for (g/mol) for each element of five different samples:

x= 0.00 mol

Total molecular weight= 45.925 g/mol

Table 3.2: Calculation of weight for each element for x = 0.00 mol

Element	Formula Weight (g/mol)	Moles	Molecular Mass (g/mol)	Mass (1.6g)
Mg	24.305	1	24.305	0.84677
B	10.81	2	21.62	0.75323
Se	78.971	0	0	0

x= 0.02 mol

Total molecular weight= 47.50442 g/mol

Table 3.3: Calculation of weight for each element for x = 0.02 mol

Element	Formula Weight (g/mol)	Moles	Molecular Mass (g/mol)	Mass (1.6g)
Mg	24.305	1	24.305	0.81862
B	10.81	2	21.62	0.72818
Se	78.971	0.02	1.57942	0.05319

x= 0.05 mol

Total molecular weight= 49.87355 g/mol

Table 3.4: Calculation of weight for each element for x = 0.05 mol

Element	Formula Weight (g/mol)	Moles	Molecular Mass (g/mol)	Mass (1.6g)
Mg	24.305	1	24.305	0.77973
B	10.81	2	21.62	0.69359
Se	78.971	0.05	3.94855	0.12667

x= 0.07 mol

Total molecular weight= 51.45297 g/mol

Table 3.5: Calculation of weight for each element for x = 0.07 mol

Element	Formula Weight (g/mol)	Moles	Molecular Mass (g/mol)	Mass (1.6g)
Mg	24.305	1	24.305	0.75579
B	10.81	2	21.62	0.67230
Se	78.971	0.07	5.52797	0.17189

x= 0.10 mol

Total molecular weight= 53.8221 g/mol

Table 3.6: Calculation of weight for each element for x = 0.10 mol

Element	Formula Weight (g/mol)	Moles	Molecular Mass (g/mol)	Mass (1.6g)
Mg	24.305	1	24.305	0.72253
B	10.81	2	21.62	0.64271
Se	78.971	0.1	7.8971	0.23476

3.3 Procedures for Sample Preparation

3.3.1 Grinding Process

The powders needed for each sample were weighed by using an electronic analytical weight balance (Figure 3.1) according to the calculations in Section 3.2. The powders of each sample were mixed and ground for at least 1 hour until homogeneous by using a mortar and pestle (Figure 3.2).

Figure 3.1: Electronic Analytical Weight Balance

Figure 3.2: Mortar and Pestle

3.3.2 Pelletization

Ground powders were weighed and separated to 0.5g per portion. They were divided into four pellets. The mould and die were cleaned by using acetone. Next, the powders were loaded into a 13mm diameter mould and pressed into a disc-shaped pellet (Figure 3.3) with 5 tons of pressure for 5 minutes by using a hydraulic press system (Figure 3.4).

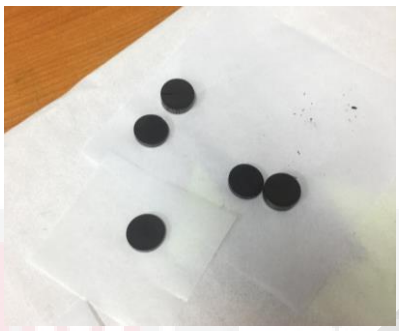

Figure 3.3: Disc-shaped Pellets

Figure 3.4: Hydraulic Press System

3.3.3 Sintering Process

The samples were ready for the sintering process after the pellets were prepared. Five pellets of each sample were loaded into a stainless-steel tube with one side of the end was sealed. After the pellets were loaded inside the tube, the other end was also sealed. The stainless-steel tube was then loaded into the furnace with Argon gas flow. One end of the furnace was connected to a water bath to ensure a constant flow of Argon gas through the furnace. Each set of samples was sintered at 800°C for 1 hour at a rate of 5°C per minute of heating and cooling. Temperature profile for the sample as shown in Figure 3.5.

The time taken to hold the sintering temperature at 800˚C is calculated as shown below:

Time = (800-30)/5

= 154 min

= 2 hours 34 mins

= 2.57 hours

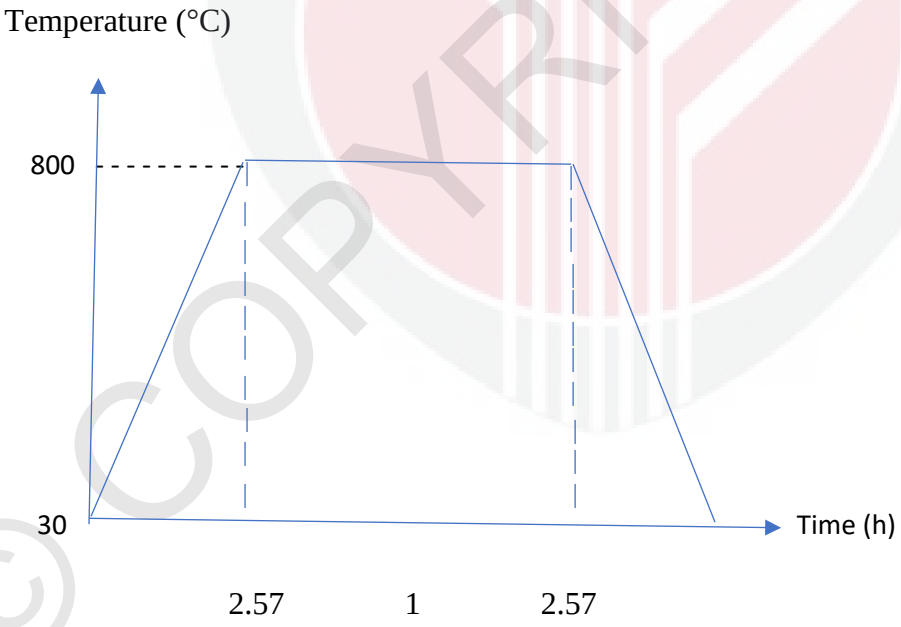

Figure 3.5: Temperature versus time for samples sintered at 800°C

3.4 Characterization

3.4.1 X-ray Diffraction (XRD)

X-ray diffraction analysis (XRD) is a technique for determining a material's crystallographic structure. XRD is a technique that involves irradiating a material with incoming X-rays and then measuring the intensities and scattering angles of the X-rays that exit the substance. The crystal structure, phase formation, crystalline phase, crystal orientation, and lattice characteristics of the materials may all be seen using XRD. X-rays are waves of electromagnetic energy, whereas crystals are regular arrays of atoms. The interaction of incident X-rays with the electrons of crystal atoms scatters incident X-rays. Elastic scattering is the name for this phenomenon, and the electron is the scatterer. The scatterers in a regular array produce a regular array of spherical waves. These waves cancel each other out in most directions due to destructive interference, but they add constructively in a few select directions, as indicated by Bragg's law:

$$2d\sin\theta = n\lambda \qquad \text{Equation 3.1}$$

Where *d* is the spacing between diffracting planes, θ is the incident angle, *n* is an integer, and λ is the beam wavelength. The diffracted X-rays are then detected and analysed.

The pelletized samples were first crushed and ground into powder after undergoing a sintering process before sending them for XRD analysis. PW 3040/60 MPD X'pert Pro Panalytical Philips diffractometer with CuK_{α}-radiation of wavelength, $\lambda = 1.5406$Å generated at 40KV and 30mA. The samples were scanned with a 0.33° step size across a range of 2θ=20-80°. The XRD spectra were analysed using X'Pert Highscore Plus and the ICDD-PDF 2 database.

3.4.2 Scanning Electron Microscopy (SEM)

A scanning electron microscope (SEM) is a type of electron microscope that uses a concentrated beam of electrons to scan the surface of a sample to obtain images. The electrons in the beam interact with the sample, generating a variety of signals that can be utilised to deduce surface topography and composition. The action of the electron beam causes the specimen's surface to emit high-energy backscattered electrons and low-energy secondary electrons. In this process, the microstructure is observed from the surface structure of the sample by using the SEM-LEO 1455 VPSEM equipped with the energy dispersive X-ray spectrometer (EDX).

Electrons are created at the top of the column, driven down the column, and focused on the sample's surface by a sequence of lenses and apertures. The sample is placed on a stage in the chamber region, and both the column and the chamber are evacuated by a combination of pumps, unless the microscope is engineered to operate at low vacuums. The placement of the electron beam on the sample is controlled by scanning coils situated above the objective lens. The beam can be scanned across the sample's surface thanks to these coils. As a result of the electron-sample interaction, several signals are produced. These pulses are then detected using detectors. A scanning electron microscope (SEM-LEO 1455 VPSEM) with an energy dispersive X-ray spectrometer (EDX) was employed in this work. To prevent electrostatic charge, the samples were coated with a tiny layer of gold before being examined microscopically as shown in Figure 3.6. The sample was then placed in the stage holder. The EDX analysis provided the micrographs of the targeted area. The image-J software was used to calculate the grain size measurement for each SEM picture.

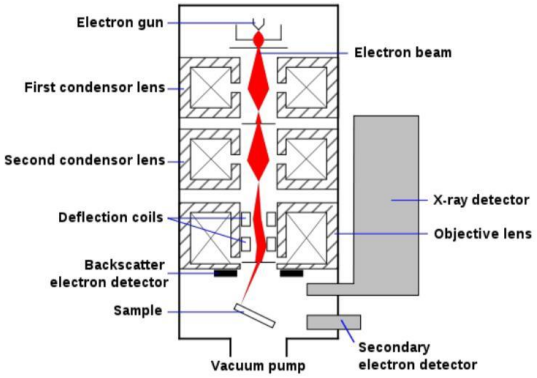

Figure 3.6: Schematic diagram of the scanning electron microscope (SEM)

(Microscope & Sem, n.d.)

3.4.3 Densimeter

Firstly, the tank is filled with 1 Litre of distilled water. The sample is placed on the densimeter to measure the mass of the sample in the air. After that, the sample is put into the densimeter which is filled with water to measure the mass of the sample in the water and the density of the sample. The cover of the densimeter must be closed every time measuring the mass and density. The step is repeated for the other samples.

Figure 3.7: Densimeter

CHAPTER 4

RESULTS AND DISCUSSION

4.1 X-ray Diffraction (XRD)

Figure 4.1 shows the XRD patterns of the MgB_2 without and with the addition of 0.02, 0.05, 0.07 and 0.10 mol of Se samples sintered at 800˚C for 1 hour. All of the series of the samples were indexed to MgB_2 of hexagonal unit cell and P6/mmm space group with $a = b \neq c$ while $\alpha = \beta = 90^{\circ}$ and $\gamma = 120^{\circ}$ (ICSD file number: 98-010-6149). As can be seen in the figure, MgO (ICSD file number: 98-011-0575), MgB_4 (ICSD file number: 98-009-1660), MgSe (ICSD file number: 98-006-2854) and Se (ICSD file number: 98-006-0972) was the impurities phase which was found to be a major phase and MgB_2 was the minor phase for all samples. The presence of MgO could be attributed to oxygen trapped during the pelletization process (Muralidhar et al., 2015). The expected impurity phase in MgB_2 is MgO which is due to the oxidation of metallic Mg (Singh et al., 2014). The MgO peaks are highly visible (white color), showing that some MgB_2 was oxidised during the sintering process and MgO was the major phase in the sintered samples (Wu, 2014). MgB_4 peaks can also be seen clearly in the XRD patterns of the pure MgB_2. Sintering MgB_2 material decomposed easily due to the volatility of Mg at high temperatures, resulting in an increase in MgB_4 phase (Savaskan et al., 2009). For the MgB_2 with the addition of Se, MgSe and Se peaks can be observed clearly.

Table 4.1 shows the intensity fraction of selected peaks of the MgB_2 without and with the addition of 0.02, 0.05, 0.07 and 0.10 mol of Se samples sintered at temperature 800˚C for 1 hour. As the addition of Se increases, the intensity fraction of MgB_2 also decreases while the intensity fraction of MgO, MgSe and Se increases. The decomposition of MgB_2 into MgB_4 is the cause of the decreased intensity fraction of MgB_2 (Savaskan et al., 2009). The increased intensity fraction for the MgO phase could be attributed to the oxidation of free Mg during the sintering process as a result of MgB_2 decomposition and due to powder handling in air, formation of MgO is unavoidable (Tan et al., 2017). It should be noted that impurities can act as flux pinning centres. The critical current density can be increased with the presence of such flux pinning centres.

Table 4.2 illustrates the crystallite size, lattice parameter and lattice strain of the MgB_2 without and with the addition of 0.02, 0.05, 0.07 and 0.10 mol of Se samples sintered at temperature 800˚C for 1 hour. The crystallite size and the lattice strain was calculated using the Williamson-Hall effect method. The five peaks with the highest intensity of MgB_2 were

chosen and plotted to determine the slope and intercept which represent the value of lattice strain and crystallite size, respectively. The crystallite size of MgB_2 increases with the increasing addition of Se but for the crystalline size for the sample x = 0.10 became smaller. Furthermore, the lattice strain of the MgB_2 without addition is higher than the MgB_2 with the addition of Se which is 0.582%. Because of its smallest crystallite size, it has the greatest peaks of the intensity value among the samples, suggesting its lowest crystallinity (Tan et al., 2017). The MgB_2 with the addition of 0.02 and 0.05 mol of Se sample showed the highest crystallite size which is 48 nm, indicating the crystallite growth. The addition of Se to the MgB_2 did not show the smallest crystallite size than the MgB_2 without addition and the size of x = 0.10 is smaller than x = 0.02, 0.05 and 0.07.

The lattice parameter of MgB_2 was determined based on the Rietveld method by using the X'pert Highscore Plus software. As can be seen in Table 4.2, the lattice parameter along the *c*-axis was higher than the *a*-axis at all samples. This is thought to be related to the fact that out-of-plane Mg-B bonds are substantially weaker than in-plane Mg-Mg bonds (Buzea & Yamashita, 2001). Longer c-axis values indicated higher oxygen substitution at the B site (Tan et al., 2017).

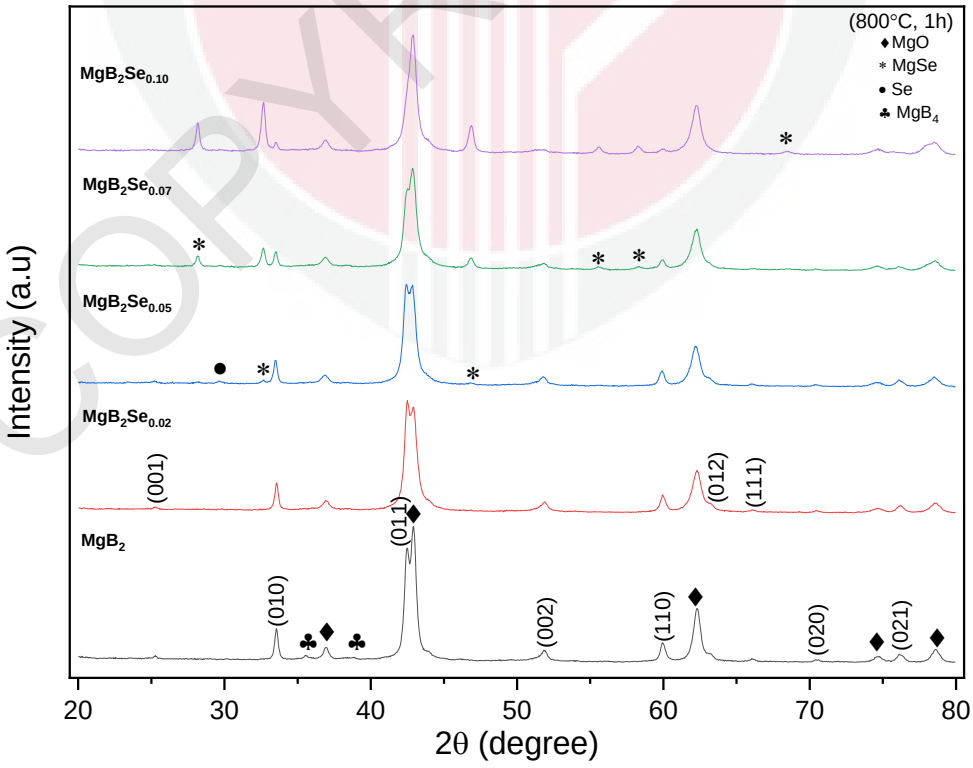

Figure 4.1: XRD pattern for each sample sintered at 800˚C

Table 4.1: Intensity fraction of selected peaks for each sample

Sample	Intensity fraction (%)		
	MgB_2	**MgO**	**Others (MgSe, Se)**
MgB_2	47.4	52.6	0
$MgB_2Se_{0.02}$	52.5	47.5	0
$MgB_2Se_{0.05}$	48.4	49.2	2.4
$MgB_2Se_{0.07}$	33.6	51.8	14.6
$MgB_2Se_{0.10}$	6.3	57.5	36.2

Table 4.2: Crystallite size, lattice parameter and lattice strain for each sample

Sample	Crystallite size (nm)	Lattice strain (%)	Lattice parameters (Å)	
			a=b	**c**
MgB_2	35	0.583	3.086	3.534
$MgB_2Se_{0.02}$	40	0.027	3.085	3.523
$MgB_2Se_{0.05}$	48	0.279	3.087	3.528
$MgB_2Se_{0.07}$	48	0.196	3.085	3.523
$MgB_2Se_{0.10}$	21	0.223	3.085	3.523

4.2 Microstructure

Figure 4.2, Figure 4.4, Figure 4.6, Figure 4.8, and Figure 4.10 display the SEM images of the MgB_2 without and with the addition of 0.02, 0.05, 0.07 and 0.10 mol of Se sintered at temperature 800˚C for 1 hour. The black, grey, and white portions in the SEM images represent voids, MgB_2, and impurity phases, respectively (Tanaka et al., 2012). As shown in the SEM images, the pure MgB_2 sample can be easily recognized compared to samples with the addition of Se. As shown in the SEM images, the sintered MgB_2 with the Se addition are porous. MgO could be white agglomerates with an uneven morphology. The production of oxide phases, particularly at the grain surface, may result in the deformed grains seen (Tan et al., 2017). The MgB_2 with the addition of Se have high porosities which slightly hard to calculate the grain size. By that, the data obtained contradict the idea that adding Se to the samples will aid in the reduction of MgO production (Guilmeau et al., 2003). It has been reported before that when the MgO content rises, the grain size decreases (Guilmeau et al., 2003).

Figure 4.3, Figure 4.5, Figure 4.7, Figure 4.9, and Figure 4.11 show the grain size distribution of the MgB_2 without and with the addition of 0.02, 0.05, 0.07 and 0.10 mol of Se samples sintered at temperature 800˚C for 1 hour. The grain size distribution was calculated using the software ImageJ. For the grain size distribution computation, 100 grains were chosen at random areas across the pellet. In each series of samples, the average grain size of the samples was found to increase with increasing the addition of Se to pure MgB_2 which the higher grain size is 0.8μm. Therefore, the average grain size of the $MgB_2Se_{0.10}$ was found to be higher than the others. Hence, it is found that the addition of Se led to grain growth.

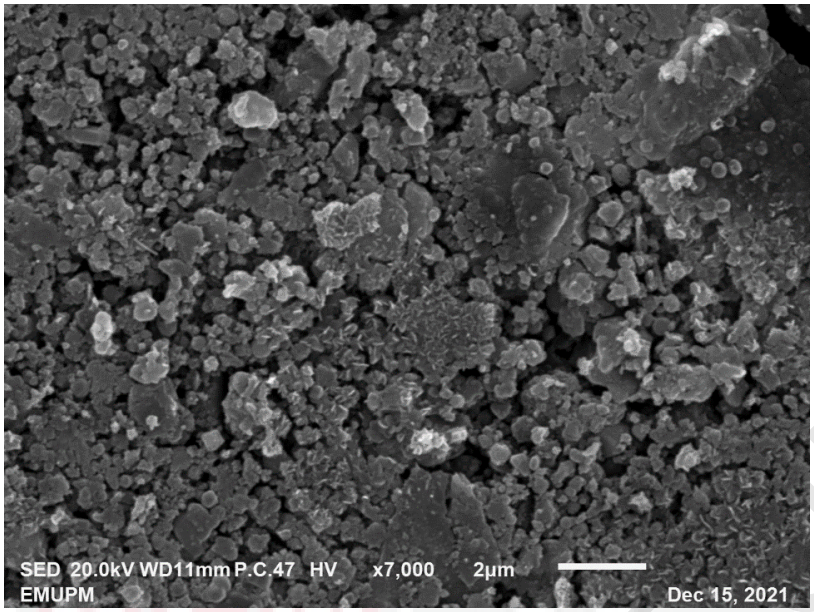

Figure 4.2: SEM images of MgB_2 sintered at 800˚C for 7000x magnification

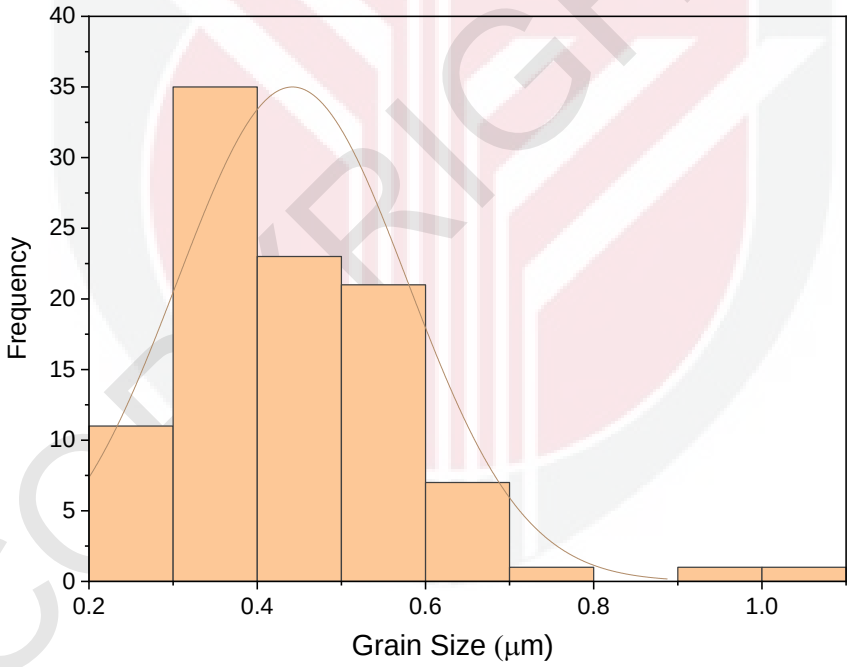

Figure 4.3: Grain size distribution of MgB_2 sintered at 800˚C.

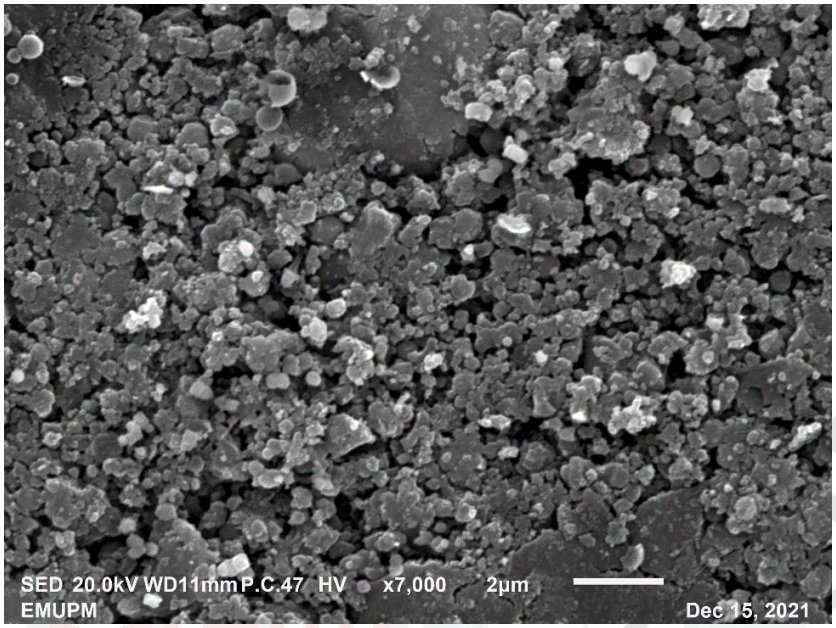

Figure 4.4: SEM images of $MgB_2Se_{0.02}$ sintered at 800˚C for 7000x magnification

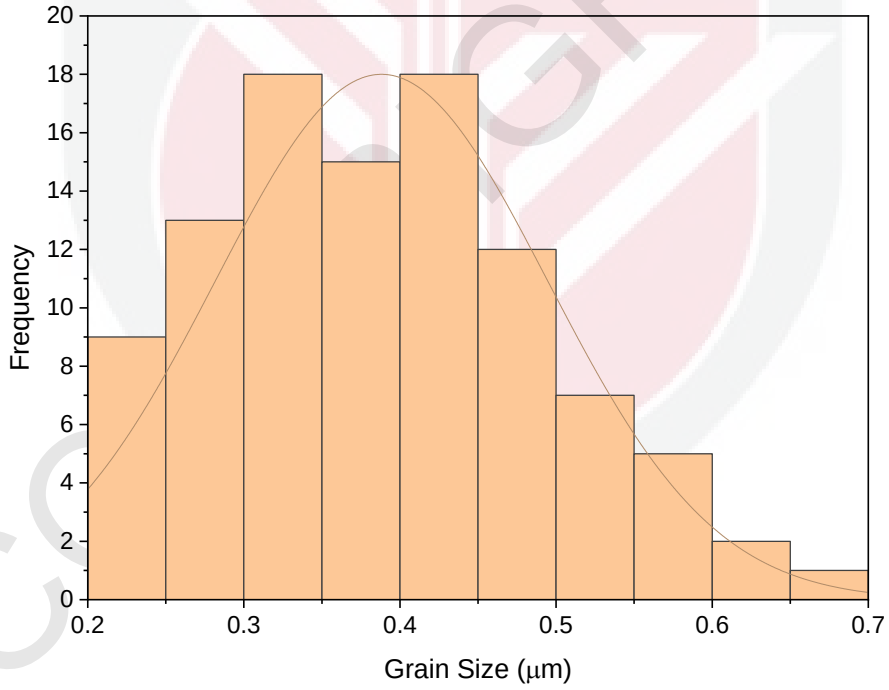

Figure 4.5: Grain size distribution of $MgB_2Se_{0.02}$ sintered at 800˚C

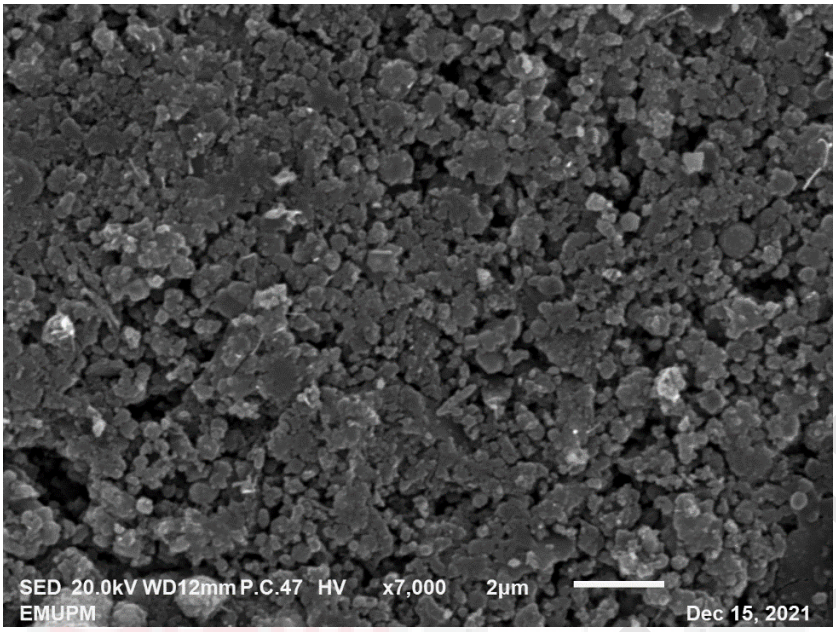

Figure 4.6: SEM images of $MgB_2Se_{0.05}$ sintered at 800˚C for 7000x magnification

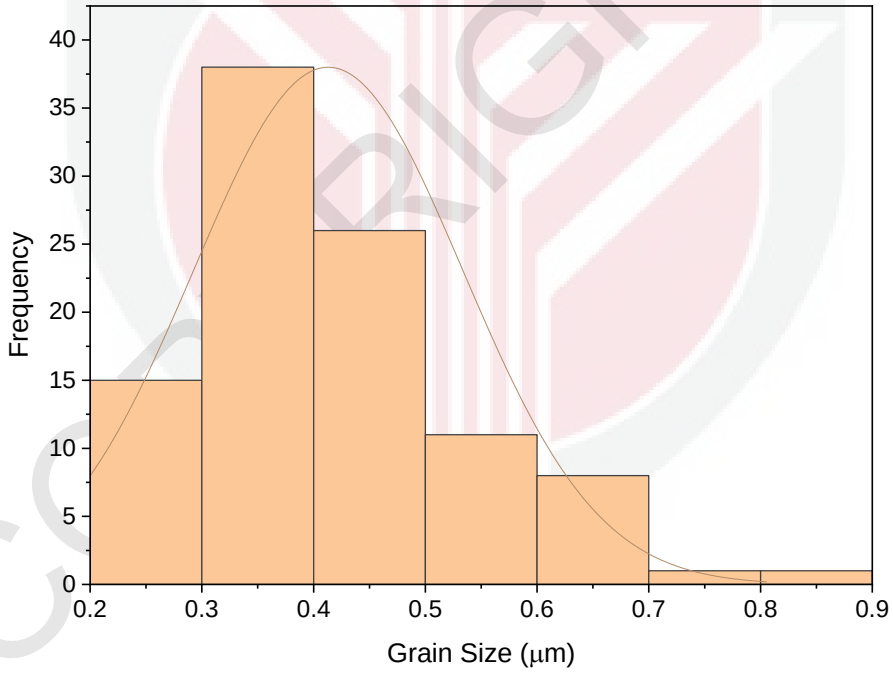

Figure 4.7: Grain size distribution of $MgB_2Se_{0.05}$ sintered at 800˚C

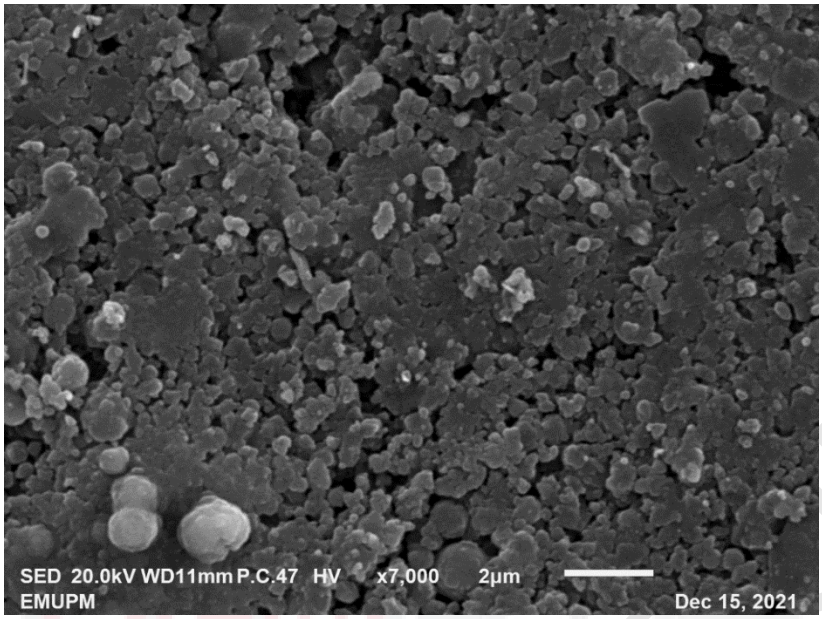

Figure 4.8: SEM images of $MgB_2Se_{0.07}$ sintered at 800˚C for 7000x magnification

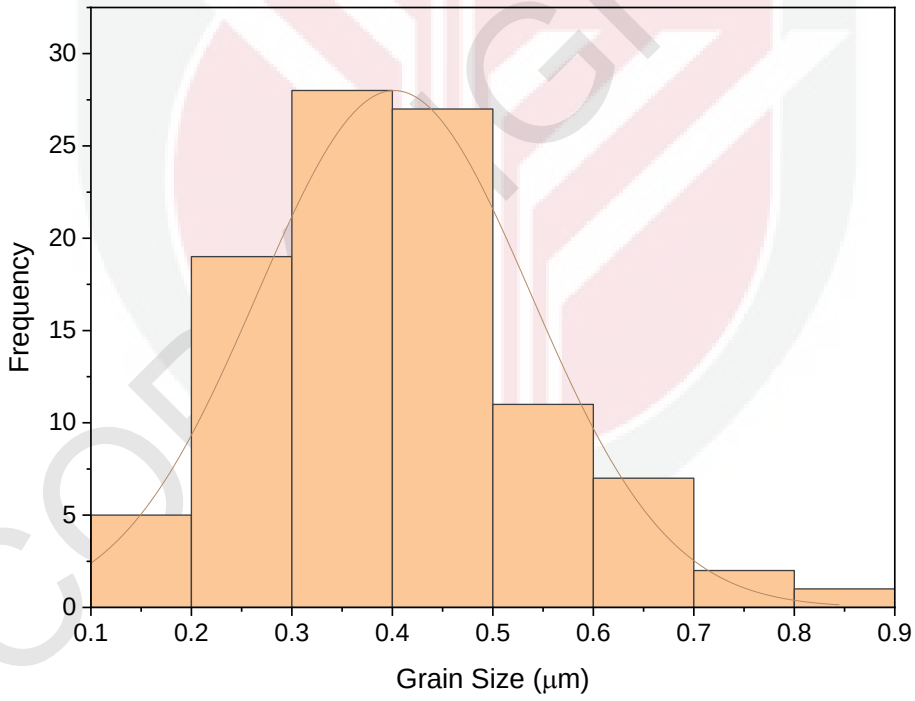

Figure 4.9: Grain size distribution of $MgB_2Se_{0.07}$ sintered at 800˚C

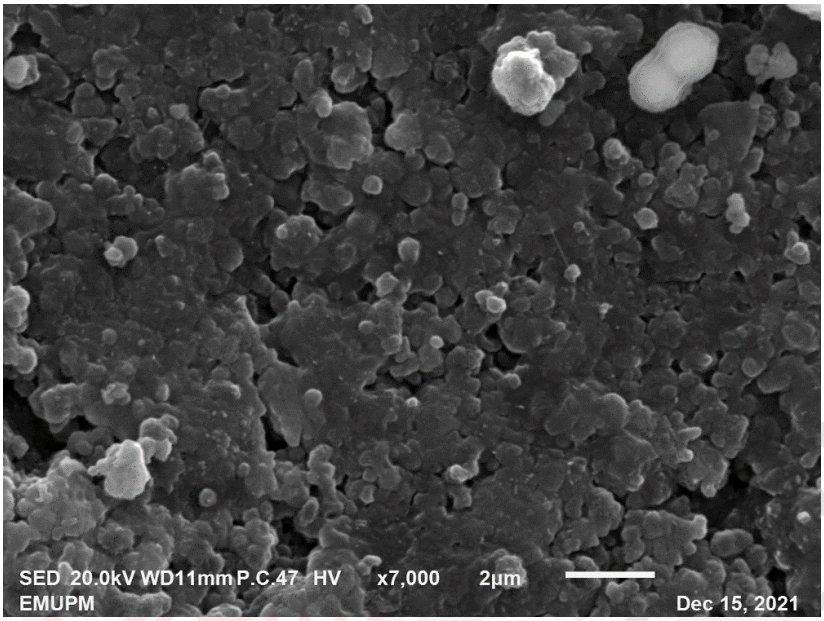

Figure 4.10: SEM images of $MgB_2Se_{0.10}$ sintered at 800˚C for 7000x magnification

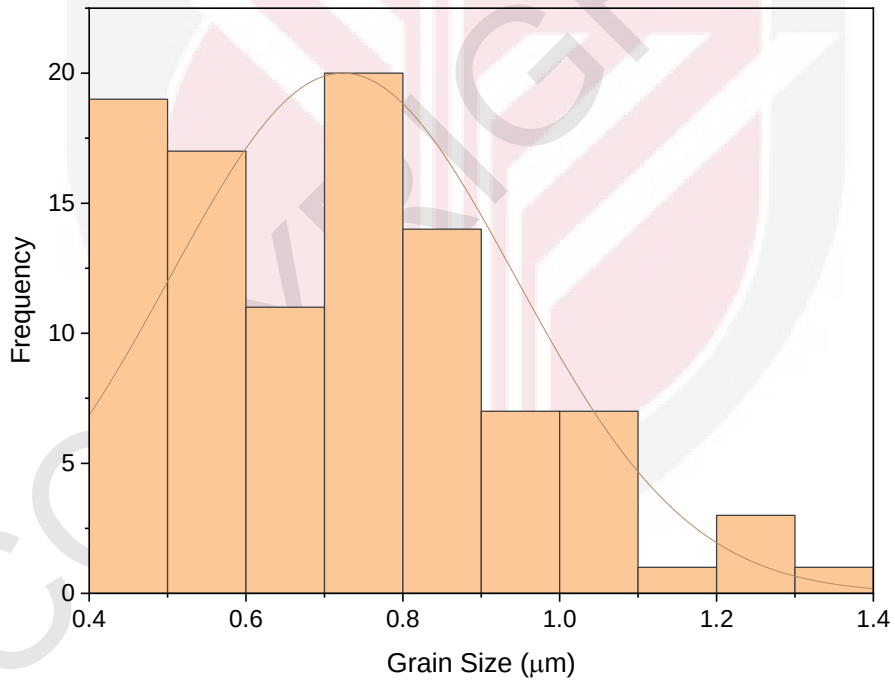

Figure 4.11: Grain size distribution of $MgB_2Se_{0.10}$ sintered at 800˚C

4.3 Density Measurement

Table 4.3 indicates the density of MgB_2 without and with Se addition of 0.02, 0.05, 0.07 and 0.10 mol, respectively. The density was obtained by using a densimeter and calculated using Archimedes' Principle. A buoyant force is experienced when an object is submerged in a fluid. This buoyant force is the result of pressure-based forces acting on the submerged object's surfaces. The buoyant force is directed upward because the pressure is higher at greater depths in the fluid (Mohazzab, 2017). The measured and calculated density of the samples was determined to be slightly the same between 1.86g/cm^3 to 1.41g/cm^3 with increasing the Se addition to the pure MgB_2.

Figure 4.15 shows the graph of density against sample for all samples. The results clearly showed that the density of samples with the addition of Se was lower than that without the Se. MgB_2's high density encourages grain connection and this could be due to a big volume of Mg evaporating, resulting in higher density of voids in the bulk (Zhang et al., 2015). The lower density of the MgB_2 may also be caused by the higher amount of MgO trapped in the samples.

Table 4.3: Density of each sample

Samples	**Mass in air (g)**	**Mass in water (g)**	**Volume (cm^3)**	**Density Measured using Densimeter (g/cm^3)**	**Density Calculated Manually (g/cm^3)**
MgB_2	0.48	0.22	0.26	1.86	1.85
$MgB_2Se_{0.02}$	0.36	0.17	0.19	1.81	1.89
$MgB_2Se_{0.05}$	0.17	0.06	0.11	1.54	1.54
$MgB_2Se_{0.07}$	0.36	0.11	0.25	1.46	1.44
$MgB_2Se_{0.10}$	0.34	0.10	0.24	1.41	1.41

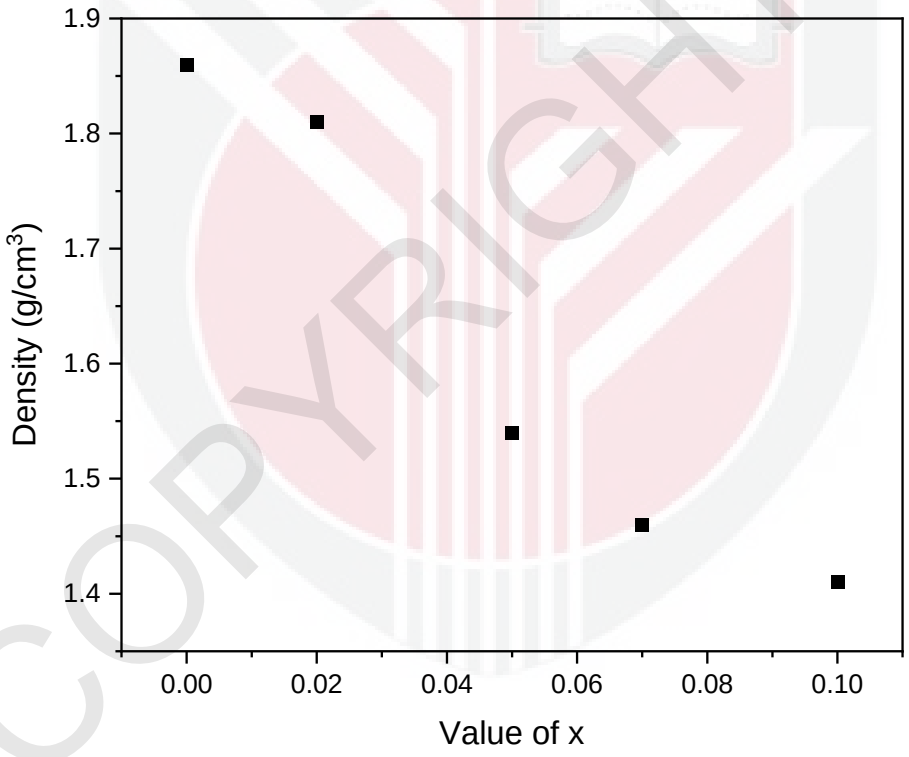

Figure 4.12: Density against the value of x

CHAPTER 5

CONCLUSION

5.1 Conclusions

In this project, five polycrystalline samples were prepared. They are pure MgB_2 and MgB_2 with x = 0.02, 0.05, 0.07 and 0.10 Se addition with the chemical formula is $MgB_2[Se]_x$. The pellets were sintered at the temperature of 800˚C for 1 hour in a constant argon gas flow environment. The samples were characterized by using the X-ray diffraction method (XRD), scanning electron microscope (SEM), four-point probe (4PP) and densimeter.

In a nutshell, it can be concluded that the dominant phase of the sintered MgB_2 without and with Se addition was MgO which showed the highest weight percentage. The minor peaks MgB_2, MgB_4, MgSe and Se were also found. Sintered MgB_2 without and with Se addition had hexagonal crystal structure and P6/mmm space group, respectively. Lattice parameters a, b, c and axial angle α, β, γ have fulfilled the requirements of a hexagonal lattice system where a = b ≠ c and α = β = 90˚, γ = 120˚ (ICSD file number: 98-010-6149). The crystallite size was found to increase with the exception of x = 0.10 while the lattice strain was decreased with increasing the addition of Se. The lattice strain of the MgB_2 without addition is higher than the MgB_2 with the addition of Se which is 0.582%. The lattice parameters *a*-axis and *c*-axis of the sintered MgB_2 without were lower than the MgB_2 with the addition of Se. The volume of the samples was almost the same which was 29Å^3.

Based on the SEM images, the hexagonal grains were more distorted and more agglomerates were found on the MgB_2 without the addition of Se. The average grain size of the samples increases with the increasing addition of Se. The grain size increased from 0.4μm to 0.8μm indicating grain growth. The density of the sintered MgB_2 without the addition of Se is higher than the MgB_2 with the addition of Se. The density was in the range of 1.86g/cm^3 to 1.41g/cm^3. The density of the MgB_2 with the addition of Se was lower due to the evaporation of a large amount of MgO which results in large holes in the bulk.

5.2 Suggestion

1) Since MgO was the major phase for this experiment, it is suggested that the samples can be carried out in a glove box with supplied of argan gas that could help to reduce the amount of oxygen trapped in the samples especially for the palletization process and sintering process.

2) The temperature for the sintering process could be varied so that we can have more data and accurate results.

3) The addition of Se should be varied to the higher amount of mol which is more than 0.10 mol to study the effectiveness of the Se addition.

4) The grain connectivity and critical current density should be measured in order to study the superconducting properties of MgB_2.

References

Aksu, E. (2013). Study of MgB_2 phase formation by using XRD, SEM, thermal and magnetic measurements. *Journal of Alloys and Compounds*, *552*(February), 376–381.

Bharat, A. (2018). Superconductors and its Applications 1. *International Journal of Pure and Applied Mathematics*, *119*(12), 7377–7386.

Buzea, C., & Yamashita, T. (2001). Review of superconducting properties of MgB2. *Cond-Mat*, *1*(1), 1–35.

De Lima, O. F. (2002). Studies on the anisotropic properties of MgB2. *Brazilian Journal of Physics*, *32*(3), 748–754.

Dewi, Y. P., Yudanto, S. D., Widyastuti, Wicaksono, S. T., Nugraha, H., & Imaduddin, A. (2018). Preparation and characterization of MgB2 polycrystalline with different milling method. *AIP Conference Proceedings*, *2*(1), 1-25.

Gill, A. S. (2018). Meissner Effect (1933) Re-Explained by Gill's Electronic Theory of Magnetism (1964). *American Research Journal of Physics*, *4*(1), 1–14.

Grivel, J. C. (2018). Influence of iridium doping in MgB2 superconducting wires. *Physica C: Superconductivity and Its Applications*, *547*, 7–15.

Grivel, J. C., Andersen, N. H., Pallewatta, P. G. A. P., Zhao, Y., & Von Zimmermann, M. (2012). Influence of Bi, Se and Te additions on the formation temperature of MgB 2. *Superconductor Science and Technology*, *25*(1), 5-9.

Guilmeau, E., Andrzejewski, B., & Noudem, J. G. (2003). The effect of MgO addition on the formation and the superconducting properties of the Bi2223 phase. *Physica C: Superconductivity and Its Applications*, *387*(3–4), 382–390.

Microscope, S. E., & Sem, C. (n.d.). *Schematic Diagram of a SEM Principle of operation :* 1–3.

Mohazzab, P. (2017). Archimedes' Principle Revisited. *Journal of Applied Mathematics and Physics*, *05*(04), 836–843.

Muralidhar, M., Nozaki, K., Kobayashi, H., Zeng, X. L., Koblischka-Veneva, A., Koblischka, M. R., Inoue, K., & Murakami, M. (2015). Optimization of sintering conditions in bulk MgB2 material for improvement of critical current density. *Journal of Alloys and*

Compounds, *649*, 833–842.

Nagamatsu, J., Nakagawa, N., Muranaka, T., Zenitani, Y., & Akimitsu, J. (2001). Superconductivity at 39 K in magnesium diboride. *Nature*, *410*(6824), 63–64.

Ravindran, P., Vajeeston, P., Vidya, R., Kjekshus, A., & Fjellvåg, H. (2001). Detailed electronic structure studies on superconducting (formula presented) and related compounds. *Physical Review B - Condensed Matter and Materials Physics*, *64*(22), 50-78.

Rowell, J. M., Xu, S. Y., Zeng, X. H., Pogrebnyakov, A. V., Li, Q., Xi, X. X., Redwing, J. M., Tian, W., & Pan, X. (2003). Critical current density and resistivity of MgB2 films. *Applied Physics Letters*, *83*(1), 102–104.

Savaskan, B., Ozturk, K., Celik, S., & Yanmaz, E. (2009). Improvement of superconducting properties of MgB2 by changing the argon ambient pressure and sintering conditions. *Journal of Physics: Conference Series*, *153*(March 2016), 1-30.

Seeger, K. (1999). Elementary Properties of Semiconductors. *Semiconductor Physics*, 1–9.

Shcherbakov. (2011). Magnesium diboride superconductor : thermal stabilization and doping. *Thesis*.

Singh, D. K., Tiwari, B., Jha, R., Kishan, H., & Awana, V. P. S. (2014). Role of MgO impurity on the superconducting properties of MgB2. *Physica C: Superconductivity and Its Applications*, *505*, 104–108.

Tan, K. Y., Tan, K. B., Lim, K. P., Jumiah, H., Halim, S. A., & Chen, S. K. (2017). Frequency dependence of dielectric properties of ex situ MgB2 bulks. *Journal of Materials Science: Materials in Electronics*, *28*(18), 13391–13400.

Tanaka, H., Yamamoto, A., Shimoyama, J. I., Ogino, H., & Kishio, K. (2012). Strongly connected exsitu MgB 2 polycrystalline bulks fabricated by solid-state self-sintering. *Superconductor Science and Technology*, *25*(11), 1-10.

Waremra, R. S., & Betaubun, P. (2018). Analysis of Electrical Properties Using the four point Probe Method. *E3S Web of Conferences*, *73*, 1–4.

Wu, F. (2014). The Improved Superconducting Properties in the Ex-situ Sintered MgB2

Bulks with Mg Addition. *Journal of Low Temperature Physics*, *177*(3–4), 157–164.

Yamamoto, A., Tanaka, H., Shimoyama, J. I., Ogino, H., Kishio, K., & Matsushita, T. (2012). Towards the realization of higher connectivity in MgB 2 conductors: In-situ or sintered ex-situ? *Japanese Journal of Applied Physics*, *51*(1), 1-40.

Yom, A. (n.d.). *The London Equations*.

Zeng, R., Lu, L., Li, W. X., Wang, J. L., Shi, D. Q., Horvat, J., Dou, S. X., Bhatia, M., Sumption, M., Collings, E. W., Yoo, J. M., Tomsic, M., & Rindfleisch, M. (2008). Excess Mg addition MgB2 /Fe wires with enhanced critical current density. *Journal of Applied Physics*, *103*(8), 1-39.

Zhang, H., Zhao, Y., & Zhang, Y. (2015). The Effects of Excess Mg Addition on the Superconductivity of MgB2. *Journal of Superconductivity and Novel Magnetism*, *28*(9), 2711–2714.